

Ultrasound-assisted decoration of CuO_x nanoclusters on TiO₂ nanoparticles for additives free photocatalytic hydrogen production and biomass valorization by selective oxidation

Dimitrios A. Giannakoudakis^{a,*}, Abdul Qayyum^a, Vaishakh Nair^{a,b}, Ayesha Khan^a, Swaraj R. Pradhan^a, Jovana Prekodravac^{a,c}, Kyriazis Rekos^e, Alec P. LaGrow^d, Oleksandr Bondarchuk^d, Dariusz Łomot^a, Konstantinos S. Triantafyllidis^{e,*}, Juan Carlos Colmenares^{a,*}

^a Institute of Physical Chemistry, Polish Academy of Sciences, Kasprzaka 44/52, 01-224, Warsaw, Poland

^b Department of Chemical Engineering, National Institute of Technology Karnataka, Surathkal, Srinivasnagar P.O, Mangalore 575025, India

^c Vinča Institute of Nuclear Sciences – National Institute of the Republic of Serbia, University of Belgrade, Serbia

^d International Iberian Nanotechnology Laboratory, Braga 4715-330, Portugal

^e Department of Chemistry, Aristotle University of Thessaloniki, University Campus, Thessaloniki, Greece

ARTICLE INFO

Keywords:

Ultrasound assisted synthesis
Hydrogen generation
Biomass photocatalytic valorization
Nano-engineered titanium dioxide
Benzyl alcohol
HMF selective photo-oxidation

ABSTRACT

The herein presented ultrasound-assisted ultra-wet (US-UWet) impregnation synthetic approach was followed in order to avoid the drawbacks of the conventional wet impregnation synthesis. The goal was to homogeneously decorate the surface of the TiO₂ nanoparticles with nanometric sized (< 4 nm) clusters of mixed cupric and cuprous oxides. The physicochemical features of the nanocomposite (TiO₂-CuO_x) were determined by high-angle annular dark-field scanning transmission electron microscope (HAADF-STEM), high-resolution transmission electron microscopy (HR-TEM), energy dispersive X-ray (EDX), X-ray photoelectron spectroscopy (XPS), powder X-ray diffraction (XRD), and Diffuse reflectance (DR) spectroscopy. TiO₂-CuO_x showed an enhanced and continuous capability to generate molecular hydrogen upon low power ultraviolet irradiation. The benchmark commercial TiO₂ P25 did not reveal any H₂ formation under these conditions. TiO₂-CuO_x presented also a high efficiency for the additives-free selective partial oxidation of two well established biomass derived model platform chemicals/building blocks, 5-hydroxymethylfurfural (HMF) and benzyl alcohol (BnOH) to the value-added chemicals 2,5-diformylfuran (DFF) and benzyl aldehyde (PhCHO), respectively. The nanocomposite showed higher DFF and PhCHO yield compared to P25.

1. Introduction

Molecular hydrogen gathers a rising academic and industrial research attention as a potential fuel of the future. The ultimate research and technological goal over the last decades towards a sustainable coverage of the fuel demands is to generate H₂ from renewable sources, and biomass can be regarded as the most abundant environmentally friendly feedstock [1,2]. Going a step further, it is of a great importance the production process also to be harmonized with the green chemistry perspectives, principally in regard to the power consumption. One of the most effective and desired H₂ formation process is by direct catalytic water splitting, which can be achieved via various methods, and

electrolysis is regarded as a promising candidate [3–5]. Even though it is feasible by this way to produce ultra-high purity H₂, the economically viability of the process is still prohibitive due to the high cost of the required infrastructure and the high electrical power consumption. Thermochemical-catalytic process for H₂ production, via for instance hydrocarbons steam reforming, is the most adapted pathway, together with pyrolysis or gasification of biomass [6]. A crucial drawback although is that in these processes, the temperature of reaction should be above ca. 700 °C.

Considering all the above, it can be concluded that the most crucial drawback arises from the high energy demand of water splitting, a highly endergonic reaction (+237 kJ/mol) [7–9]. To overcome this high

* Corresponding author.

E-mail addresses: dagchem@gmail.com (D.A. Giannakoudakis), ktrianta@chem.auth.gr (K.S. Triantafyllidis), jcarloscolmenares@ichf.edu.pl (J.C. Colmenares).

<https://doi.org/10.1016/j.mcat.2021.111664>

Received 19 April 2021; Received in revised form 16 May 2021; Accepted 18 May 2021

Available online 7 June 2021

2468-8231/© 2021 The Authors.

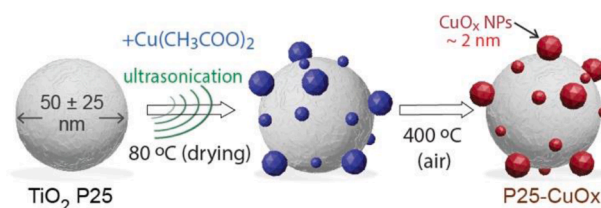
Published by Elsevier B.V. This is an open access article under the CC BY-NC-ND license

(<http://creativecommons.org/licenses/by-nc-nd/4.0/>).

energy demand, the utilization of renewable sources can be the solution, with solar energy to be assumed among the best candidates [10–13]. Towards this direction, photocatalytic H₂ generation approaches are regarded as an open field of glory and the utilization of a proper semiconductor photocatalyst, the most vital part [14–20]. In general, the absorbed electromagnetic irradiation leads to the photoexcitation of an electron from the valence band (VB) to the conduction band (CB), leaving behind a hole at the VB [21,22]. The electrons can reduce a compound, while the holes oxidize it [21,22]. TiO₂ is known of having an enhanced photocatalytic capability [23]. A key drawback although is that the band gap of the predominant polymorphs (anatase, brookite, or rutile) is quite big (3.0–3.4 eV), so UV light photo-activate TiO₂ more readily. Additionally, the lifetime of the photogenerated charges is too short, hence the most essential aspect in TiO₂-based photocatalysts design is to confine the e⁻/h⁺ recombination [24]. The deposition of nanosized phases on the titanium oxide particles or the incorporation of defected sites as well as the formation of composites with carbonaceous materials like graphene-derivatives are well-established approaches to overcome the above-mentioned limitations [11,25–32]. Especially for H₂ photo-assisted generation, the TiO₂-based materials using noble metals (particularly Pt or Au) for the surface decoration by nanoclusters are assumed as benchmark photocatalyst, although of a high cost [33–35]. Furthermore, the use of lower cost non-noble metals may also lead to similar photocatalytic efficiencies [22]. The addition of the metal nanoparticles induces a better light absorption efficiency and transfer of the photoinduced electrons, leading to a higher reducing activity and preventing the fast recombination of the photoinduced e⁻/h⁺ pairs by their delocalization within the different in chemical nature parts of the nanomaterial and/or due to the incorporation of a Schottky barrier level between the valence and conduction energy levels [21].

Among the various non-noble metals utilized, copper showed to lead to the most pronounced photoreactivity enhancement. For instance, Castañeda et al. [18] showed that CuO supported on fluorinated TiO₂ showed an elevated photocatalytic H₂ production from a water/methanol solution, and Montoya et al. [36] that other metals, like Co²⁺ and Ni²⁺, can be also used towards this direction, although with a significant lower effect compared to Cu. Clarizia and co-workers showed that photo-deposition of zero-valent copper nanoparticles (of around 30 nm in size) on commercially available Degussa TiO₂ (P25) nanoparticles had a clear positive influence on photocatalytic H₂ generation upon irradiation by a high-pressure mercury vapor lamp (125 W), due to the localized surface plasmon resonance (LSPR) effect [37]. They determined by utilizing a variety of organic compounds as the sacrificing agent that the best performance was achieved by glycerol, followed by methanol with a small difference in H₂ production efficiency. J. Yu and J. Ran incorporated different amounts of Cu(OH)₂ clusters on P25 by precipitation, using copper nitrate as precursor. The modified materials showed a high rate of H₂ formation upon irradiation of ultraviolet (365 nm) produced by four UV-LEDs (3 W), with the optimal loading to be 0.29 mol% of Cu(OH)₂ [38]. The most followed synthetic approaches are based on precipitation, photo-deposition and conventional wet impregnation (WI) in which the minimum volume of a solvent is used in order to fill the pores of the material. Although, the latter results many times to inhomogeneous agglomeration of the copper clusters on the TiO₂ surface and this had a negative effect on the availability of the active catalytic sites and on a faster catalyst' deactivation [39].

The main objective of the present work was to design a novel and low-cost TiO₂ based photocatalyst in order to eliminate the above-mentioned limitations of WI. Towards this direction, our nanocomposite's design strategy (Scheme 1) was focused on the uniform and homogeneous decoration of TiO₂ P25 nanoparticles with ultrananometric size (< 4 nm) nanostructured oxide(s) of the earth-abundant 3d transition metal, copper. To achieve this, we established an ultrasound-assisted ultra-wet (US-UWet) impregnation synthetic protocol followed by moderate temperature calcination (400 °C) and using copper acetate as the source of Cu. Emphasis was given on



Scheme 1. The design strategy based on ultrasound-assisted ultra-wet (US-UWet) impregnation synthetic protocol to decorate copper nanoclusters on titanium dioxide (TiO₂-P25/CuO_x).

studying the physicochemical features of the obtained nano-photocatalyst. Since our ultimately goal was the photocatalyst to be efficient for H₂ production under low power light irradiation using methanol as sacrificing agent and to monitor qualitatively in real time the product gasses of the reaction, we built a simple photoreactor which had the LED light source immersed in the reaction dispersion and was connected directly to a GC-TCD. Last but not least, we explored the multifunctionality of our catalyst by studying its photocatalytic efficiency for the additives-free selective partial oxidation (SPOx) of two well established biomass derived model platform chemicals/building blocks, 5-hydroxymethylfurfural (HMF) and benzyl alcohol (BnOH) to the value-added chemicals 2,5-diformylfuran (DFF) and benzyl aldehyde (PhCHO), respectively. HMF and BnOH are assumed as attracting industrially platform compounds that can be obtained from a widely available natural and renewable resources, biomass, and can be converted to added-value chemicals and products [40–43].

2. Experimental

2.1. Materials

All the chemicals and materials were used as received: TiO₂ (P25, Evonik), copper(II) acetate monohydrate (abcr GmbH; ACS, 98–102%), HPLC grade acetonitrile (AcN, POCH Avantor Performance Materials Poland S.A), 5-hydroxymethylfurfural (HMF, Chempur), 2,5-diformylfuran (DFF, Acros Organics), benzyl alcohol (BnOH), and benzyl aldehyde (PhCHO). MilliQ water was used in all cases.

2.2. Synthesis of the photocatalyst

The P25-CuOx photocatalyst was prepared following an ultrasound-assisted ultra-wet (US-UWet) impregnation approach, using TiO₂ P25 Evonik as the support. The synthetic protocol (Fig. 1) was the following: The calculated amount of copper(II) acetate monohydrate precursor (75 mg) was dissolved in 10 mL of water by the use of 2 min ultrasonication. Then, the solution was used to impregnate 1.425 g of TiO₂ P25. The obtained slurry was further sonicated inside a bath for 5 min (Sonorex-digital RC, 37 kHz, 120 W) and afterwards was dried for 16 h at 80 °C. The obtained bright bluish material was ground using an agate mortar towards a fine and homogeneous powder. The mass-yield up to this stage was 98.7% (1.4801 g of blue powder). Finally, the blueish powder was calcined in a muffle furnace under air at 400 °C for 4 h (heating ramp 10 °C/min). The finally obtained brown/gray material is referred to as P25-CuOx. The solid yield of the after calcination was found 97.1%. Assuming that the final decorated phase would be CuO, the targeted amount of CuO nanoparticles per mass of the final obtained catalyst was ~2 wt%. The pristine TiO₂ P25 Evonik is referred to herein after as P25, while the calcinated under air at 400 °C counterpart as P25-400 (Fig. 2).

2.3. Materials characterizations

The high-resolution transmission electron microscopy (HR-TEM) and scanning transmission electron microscopy (STEM) with energy

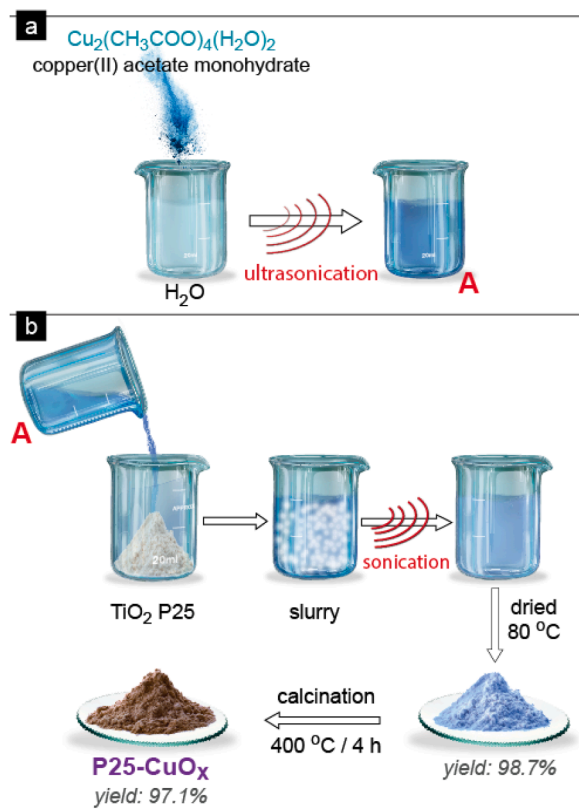


Fig. 1. A schematic representation of the entire ultrasound-assisted ultra-wet (US-UWet) impregnation synthesis TiO_2 P25- CuO_x .

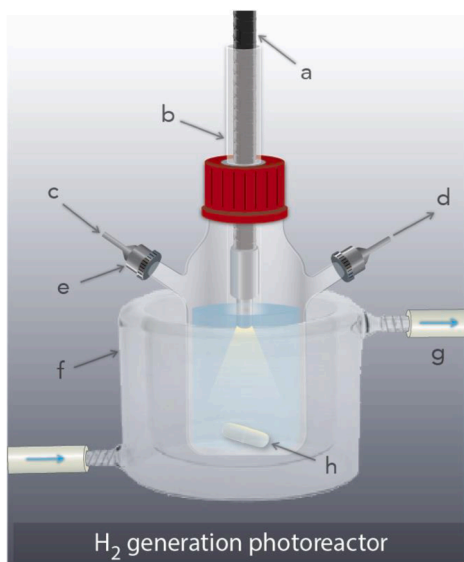


Fig. 2. Schematic illustration of the H_2 generation photoreactor where: a) LED light source (optical fiber), b) borosilicate glass tube, c) inert gas inlet, d) product gasses directly connected to GC for real-time monitoring, e) capillary connector, f) temperature controlling water bath, g) circulating water outlet, and h) magnetic stir bar.

dispersive X-ray (EDX) spectroscopy for elemental mapping were carried out on a Model Titan Themis 60–300 equipped with a Cs image and probe corrector and a Super-X EDX system operating at 200 kV. The samples for the electron microscopy analysis were prepared by depositing drops of ultrasonicated suspension of the catalyst in ethanol onto

400 mesh gold grids coated with lacey carbon supports (EM Resolutions Ltd.) after the powder were dispersed in ethanol under ultrasonication. The powder X-ray diffraction (XRD) patterns were obtained using a Siemens D5000 diffractometer (40 kV and 40 mA) equipped with a horizontal goniometer (details regarding the determination of the crystallographic parameters can be found elsewhere [44]). Diffuse reflectance (DR) spectra were obtained in the range from UVB up to near infrared by a Jasco V-570 spectrophotometer which was equipped with an integrating sphere (Spectralon [poly(tetra- fluoroethylene)]) as the baseline [45,46].

X-ray photoelectron spectroscopy (XPS) experiments were carried out in an ultra-high vacuum (UHV) system ESCALAB250Xi (Thermo Fisher Scientific). The base pressure in the system was below $5 \cdot 10^{-10}$ mbar. The XPS spectra were acquired with a hemispherical analyzer with pass energies 20 eV and 200 eV for high resolution and survey spectra, respectively. The XPS spectra were generated by a twin Al/Mg anode non-monochromated X-ray sources operated at 15 keV and power 300 W. XPS spectra were peak-fitted using Avantage (Thermo Fisher Scientific) data processing software. For peak fitting Smart-type background subtraction was used. Quantification has been done using sensitivity factors provided by Avantage library. The surface pH was determined by dispersing 0.1 g of the powder to 50 mL deionized water inside a well-sealed glass beaker and measuring the pH after 16 h of stabilization after stirring in the dark.

2.4. Hydrogen photocatalytic generation and products analysis

2.4.1. Specification of the H_2 production reactor

The herein designed homemade photocatalytic reactor for H_2 production (H2-rctr) offered the capability to tune and optimize, apart from the basic catalytic parameters (catalyst loading, concentrations, mixing rpm, duration etc.), the following crucial experimental parameters as well: i) light source frequency and power ii) temperature of the reactor, iii) the inert gas and its flow rate, and iv) the volume of solvent/dispersion in which the reaction would take place, ranging from few mL and up to 50 mL. In addition, the position of light irradiation, i.e. either inside the dispersion or above its surface and as a result the light diffusion, could be easily controlled. The usage of the capillary type connectors eliminate the possibility of leakage, while they provide also protection against overpressure inside the reaction vessel or at the entire setup. The most important feature offered from the design was the capability to continuously monitor the reaction evolution in real-time, since the outlet gas flow was directly connected with a gas chromatograph. The entire setup of the H2-rctr with descriptions of all the parts can be seen in Figure S1. The reactor can be placed on a magnetic stirrer or be immersed inside an ultrasound bath.

In this work, Argon was used as the inert gas with a flow rate of 20 mL/min. The solvent was a mixture of water and methanol (as the sacrificing agent) of 1:1 vol ratio. In order to minimize the dead-volume of the headspace above the dispersion, the volume of the solution was 50 mL, and the amount of the powder was 50 mg (i.e., 1 g/L) for each photocatalytic experiment. The borosilicate glass tube, in which the light source/optical fiber was placed inside, was immersed within the solvent at 0.5 cm depth. The reaction vessel was covered with 3 layers of aluminum foil during all the tests.

The light beam at the herein reported results was irradiated by a LED-based source (45 mW, Omikron laserage, LEDMODx.450.V2, Rodgau, Germany), emitting at 365 nm. The power of the irradiated light beam was determined as 95 W/m^2 , using a Photo-Radiometer (Delta OHM Model HD2302.0 LightMeter) equipped with a probe (Delta OHM, LP 471 UVA Probe, spectral range: 315–400 nm). The emission spectra of the utilized light beam can be found elsewhere [47].

2.4.2. H_2 production monitoring

A gas chromatograph with thermal conductivity detector (Agilent 7820A GC-TCD) was used for the analysis of the product gasses/outlet

stream from the H2-rctr. The GC parameters of the analysis protocol were oven temperature 60 °C (hold time 10 min), ramp to 110 °C (rate 25 °C/min) and hold time 2 min (total 14 min run time). For the herein reported results, the Ar flow where set at 20 mL/min using a mass flow controller (maximum up to 75 mL/min). The calibration curves were obtained by measuring mixtures of H₂ with argon. Photolysis (PL) tests were also performed.

2.5. HMF and BnOH photooxidation and analysis methods

The materials' photocatalytic activity for the selective partial oxidation of 5-hydroxymethylfurfural (HMF) to 2,5-diformylfuran (DFF) and of benzyl alcohol (BnOH) to benzyl aldehyde (PhCHO) was evaluated using the photoreactor setup as can be seen in Figure S2. The initial concentration of HMF or BnOH was 1 mM in acetonitrile. 15 mg of the catalyst powder (1 g/L) and 15 mL of the HMF or BnOH solution (1 mM) were inserted to the glass vial and the light source was applied from the top using also a cap. The reaction was held under constant magnetic stirring (600 rpm) during the whole experiment. Prior to light illumination, stabilization/equilibration was established for 1 h in the dark under continuous stirring (600 rpm). Samples of 0.2 mL were collected for analysis after specific interval of time via the sampling port using a syringe (1.5 mL) and then were immediately filtrated by syringe filter (pore size of 0.20 μm) in order to be analyzed. The temperature was maintained stable at 30 °C during all the process using water bath. The utilized light source was the same UV-LED as above-mentioned. All the experiments were performed more than three times and the standard deviation/error was less than 3%. The oxidative efficiency of the materials in the dark was also explored, while photolysis tests were also conducted.

The analysis of the samples for the BnOH photooxidation experiments was performed by a gas chromatograph equipped with flame ionization detector (Shimadzu GC-2010) using a capillary column (ZB-5MS, 30 m length, 0.25 mm inner diameter, 0.5 μm film thickness). The chromatograms were obtained by injecting 1 μL of the samples with a split ratio of 8. The column temperature was set at 50 °C for 3 min and increased up to 300 °C at a rate of 9 °C/min with a final holding time of 2 min. Helium was used as a carrier gas. The concentrations were estimated using calibration curves (details can be found at the Supplementary Information).

The product analysis in the case of HMF photooxidation was carried out on an Acquity Arc Waters HPLC instrument with 2998 PDA detector.

HMF and DFF were well separated by a C18 Thermo scientific column (250×4.6 mm). The compounds were detected by a UV detector at 270 nm. The mobile phase was composed of acetonitrile and Milli Q water with 55:45 vol ratio. The flow rate was set at 1.0 mL/min and the temperature of column oven was kept at 25 °C. The retention time of HMF and DFF was 2.6 and 3.7 min, respectively. The concentration of HMF and DFF was determined by the external standard calibration method. The same formulas as above were used for the calculation of the HMF, DFF, and FDCA concentrations.

3. Results and discussion

3.1. Physicochemical characterizations

The high-angle annular dark-field scanning transmission electron microscope (HAADF-STEM) image in Fig. 3a revealed that the TiO₂ P25 nanoparticles are decorated with nanoscaled copper-containing clusters (< 4 nm) with an average size of 1.8 nm (brighter spots indicative of the higher Z contrast of copper compared to Ti). The homogeneous deposition of the copper containing nanoclusters can also be observed from the high-resolution transmission electron microscopy (HR-TEM) images (Fig. 3b-d). The chemical nature of the nanoclusters can be validated from the EDX elemental mapping analysis (Fig. 3e-i) in which copper derived spots are clearly observable. Statistical analysis of the nanoclusters' diameter distribution based on the HR-TEM images (Figure S3) showed an average diameter of 1.68 nm, a value that agrees with the HAADF-STEM analysis.

The most challenging aspect was to verify the crystallographic and chemical nature of the copper containing nanoparticles. The surface chemistry analysis was conducted by X-ray photoelectron spectroscopy (XPS). For P25-Cu_x, the peak centered at 458.7 eV (Fig. 4) observed at the high resolution spectra for Ti 2p_{3/2} is linked to the binding energy of Ti⁴⁺, in consistence with previous reports for TiO₂ P25 [27,48–51]. The deconvolution of the high-resolution core energy level O 1s spectrum of TiO₂ P25 revealed three contributions, with maxima at 529.9, 531.2, and 532.1 eV [52]. The first one can be assigned to the surface oxide lattice O (Ti–O), the second to the acidic bridging or/and terminal hydroxyl groups (Ti–OH), and the third to the basic terminal hydroxyl groups linked to the adsorbed water moieties [53–56]. Considering also the high carbon content/impurities on the surface [27,52], the binding energies at 532.4 and 531.2 eV can also arise from the C–O and C=O bonds, respectively [56,57]. In the case of P25-Cu_x, three predominant

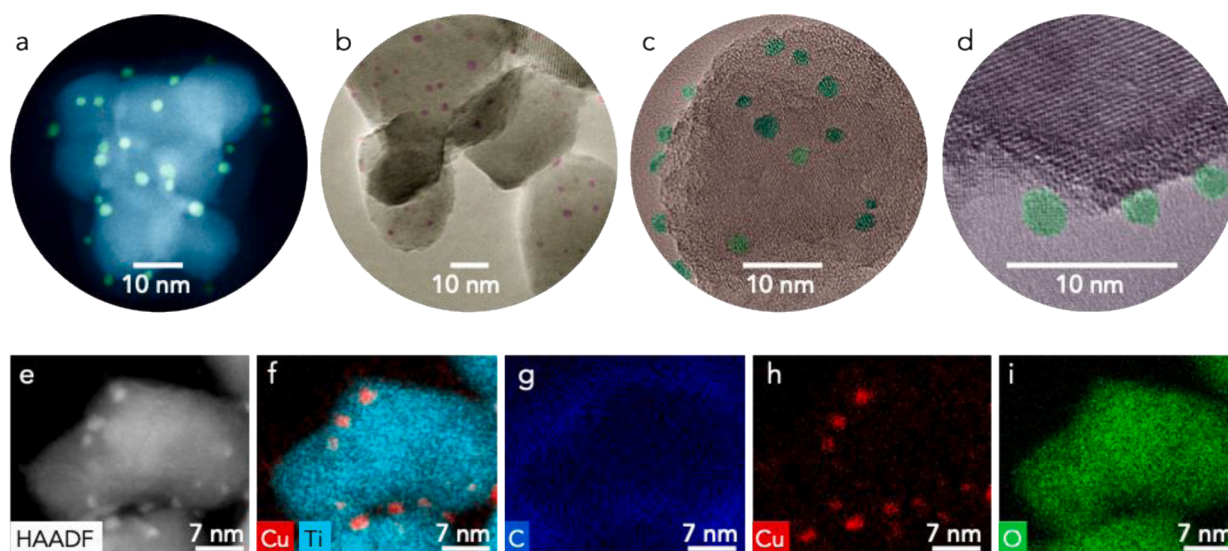


Fig. 3. High-angle annular dark-field Scanning transmission electron microscope (HAADF STEM) image (a), high resolution TEM images (b-d), and elemental mapping analysis by EDX (e-i) of P25-CuO_x (the original images can be found at the Supplementary Information).

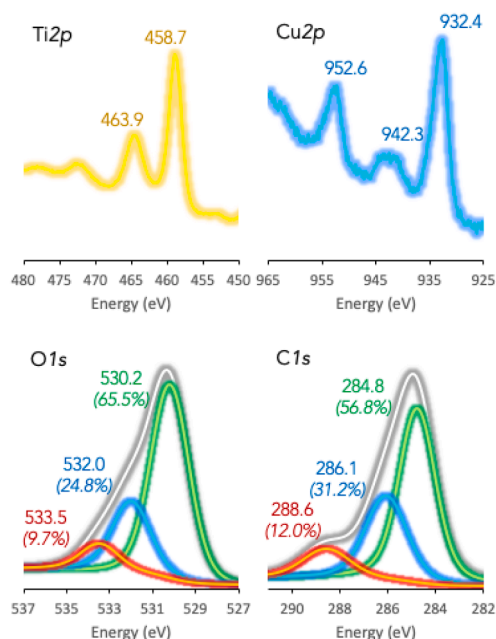


Fig. 4. XPS high-resolution deconvoluted core energy level spectra of Ti 2p, Cu 2p, O 1s, and C 1s for P25-CuO_x.

peaks were appeared at 530.2, 531.0, and 533.5 eV (Fig. 4). The surface deposition led to the shift of the binding energies of the hydroxyl surface moieties to a higher energy comparing to pristine P25, as well as in an increase of their content to 34.5% for P25-CuO_x (from 15.9% for P25). The C 1s core energy level deconvolution of P25-CuO_x revealed three kind of carbon containing functionalities centered at 284.8 eV (for adventitious carbon), 286.1 eV (for C—O bonds), and 288.6 eV (for C=O bonds) [58,59]. The same functionalities were detected in the case of P25 [52], although the ratios of the C—O and C=O bonds were almost half comparing to P25-CuO_x.

The Cu 2p core-energy level spectra revealed a dominant broad contribution between 937.1–930.1 eV, with the maximum to be at 932.4 eV. This can be linked to the presence of either Cu⁺ as Cu₂O or metallic Cu⁰. Since their binding energy values are similar, the distinction (even analyzing the Cu LMM Auger spectra) was not achievable, as reported previously for similar materials [39]. The presence of a satellite broad peak at 942.3 eV, in combination with the Cu 2p_{3/2} shake-up can be assigned to the presence of CuO, being however of relatively low contribution. Considering the above, it can be suggested that copper on the surface of TiO₂ nanoparticles exists with three different valences, 0, +1, and +2, with the latter two being the predominant ones. The Cu₂O and CuO deposited phases is also possible to be formed by oxidation of Cu⁰ upon exposure to air [39]. The elemental analysis by XPS (Table S1) showed a 2.0% atomic content of Cu (6.5 wt%). The incorporation of the nanoclusters led to a slight increment of the surface pH, from 6.1 for P25 to 6.3 for P25-CuO_x.

In order to shed light on the nature of the deposited copper-based nanoparticles, powder XRD analysis was conducted. The pattern (Fig. 5a) of P25 showed the presence of two crystalline phases, anatase (86%) and rutile (14%), and based on the Scherrer analysis, the average crystallite sizes were found 17.5 and 23.6 nm for anatase and rutile, respectively. Thermal treatment at 400 °C did not cause any alteration on the materials crystallinity. The patterns of the two allotropic structures of TiO₂ in the case of copper modified sample were presented identical as the ones of the precursor P25; only a small increment of the average crystallite size of anatase by 0.3 nm was observed. With regard to the reflections assigned to possible crystalline phases of the deposited Cu-based nanoparticles, not overlapping with those of TiO₂ (Fig. 5b), none of the metallic Cu⁰ predominant diffraction peaks of (111), (200)

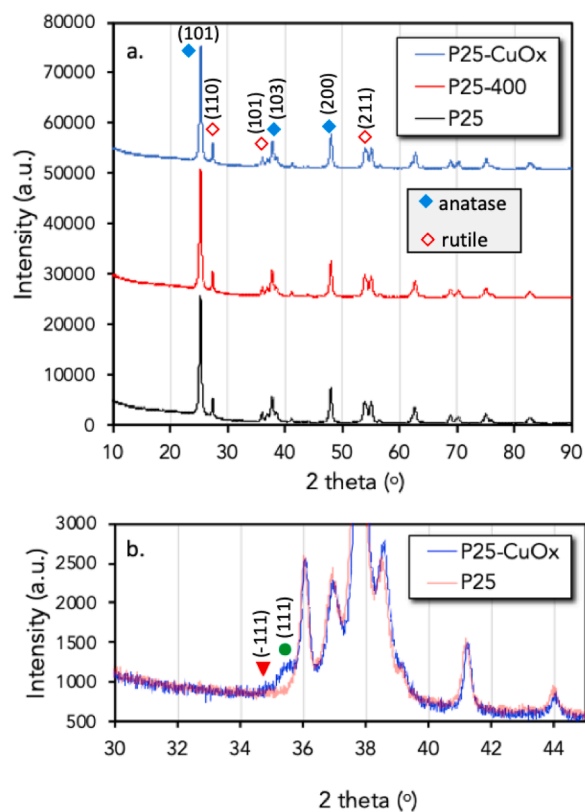


Fig. 5. XRD patterns for TiO₂ P25, P25-400, and P25-CuO_x (a) and closer captions (b), where (●) represents the cubic structured of Cu₂O cuprite and (▼) the monoclinic structured of CuO phases.

and (200) planes at 2θ 43.6°, 50.7° and 74.45° (JCPDS No. 85–1326), respectively, were detected [60,61]. On the contrary, a weak and broad reflection at 35.7° 2θ that is indexed to the (111) plane of standard cubic cuprite Cu₂O structure (JCPDF No. 78–2076) [60,61] was clearly identified. Additionally, two reflections at 35.5 and 32.5° 2θ, of very low intensity, were also detected and indicated the presence of the (−111) and (110) planes of monoclinic structure of CuO (JCPDS No. 80-1917) [61–63]. The crystallite size of the Cu₂O phase was estimated to around 4.5 nm, with a high level of uncertainty due to the very low intensity of these signals. The crystallite size of the CuO cannot be determined based on XRD due to the low signal intensity.

The optical properties were explored by diffuse reflectance (DR) spectroscopy in a wide range of the electromagnetic spectrum, from UVB up to near infrared (Fig. 6). As it is well known, P25 absorb light in the ultraviolet region, from 400 nm and below. The incorporation of the surface deposited CuO_x nanoclusters led to a coloring of the TiO₂ powder because of light absorption at the entire visible light region in addition to the ultraviolet. The optical in-direct band gaps were approximately estimated based on the linear extrapolation of the Tauc plots (Fig. 6b) derived from the Kubelka-Munk method [64,65]. For P25, the band gap was around 3.4 eV, a value in a good correlation with those reported in the literature [66]. For P25-CuO_x, the band gap was found lower by ~0.2 eV. It should be mentioned that P25-400 showed exactly the same light absorption behavior as P25.

3.2. Photocatalytic H₂ generation

Within our goals was to explore the H₂ formation capability of the new photocatalyst under low power ultraviolet (UV, 365 nm) irradiation generated from a LED source and by using the simple photoreactor setup (H₂-rctr) as described in detail in the experimental part, with methanol serving as a sacrificial oxidant. The evolution of H₂ production can be

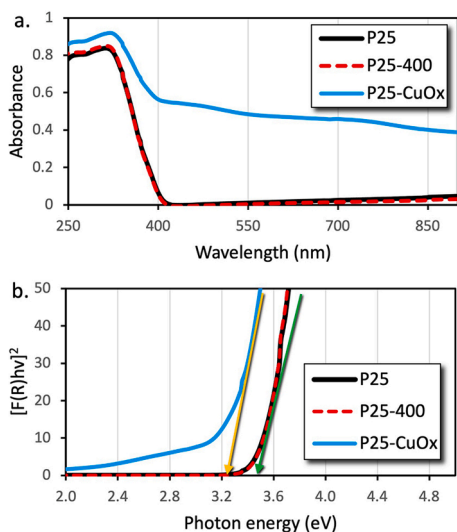


Fig. 6. Diffuse reflectance UVA to NIR absorption spectra (a) and Tauc plots (b) for TiO₂ P25, P25-400, and P25-CuOx.

seen in Fig. 7. Only P25-CuO_x was capable for the photocatalytic H₂ production, while P25 or P25-400 did not exhibit any H₂ formation. It should be pointed out that H₂ formation was also not observed during the photolysis tests. We tested also several other TiO₂ based materials, such as the commercially available TiO₂ P90, ultrasound hydroxylated TiO₂ P25 [27], grafted core-shell titania [52], titania nanotubes pure or doped with Cu, Zn, Fe nanoparticles solely or in combination, as well as various composites of the above with reduced graphite oxide [27]. None of the above showed any H₂ generation capability. For P25-CuO_x, the photocatalytic H₂ formation rate reached a maximum value initially (30 min) followed by a slight decrease towards a plateau after 120 min, a trend also observed in previous reports [37]. After the first 30 min of UV irradiation, the maximum recorded flow of produced H₂ was 2.48 μmol h⁻¹ g⁻¹ after 30 min and stabilized at 1.85 μmol h⁻¹ g⁻¹ after 2 h. This value is significant high considering the low light intensity, a feature important towards real-life application to utilize the UV range of solar light even during a cloudy day.

A marked change in color of the liquid phase was observed after some minutes of light exposure. The initial white in color colloidal suspension (Fig. 8a) was turned to purplish (Fig. 8b), suggesting that redox reaction of the copper moieties took place. Analysis of the liquid phase after the experiments did not show any leaching of Ti or Cu, thus revealing the stability of the photocatalyst. The suspension was then left

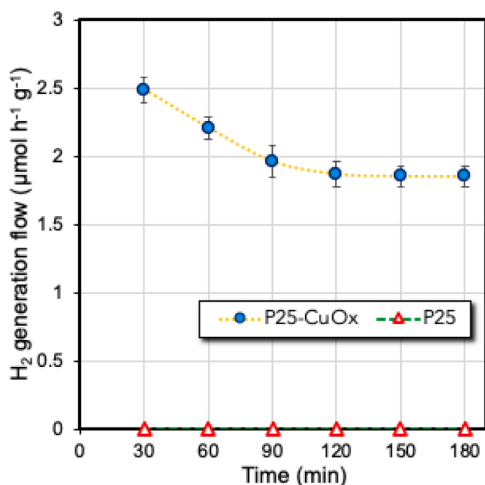


Fig. 7. The evolution of H₂ generation using P25-CuOx as photocatalyst.

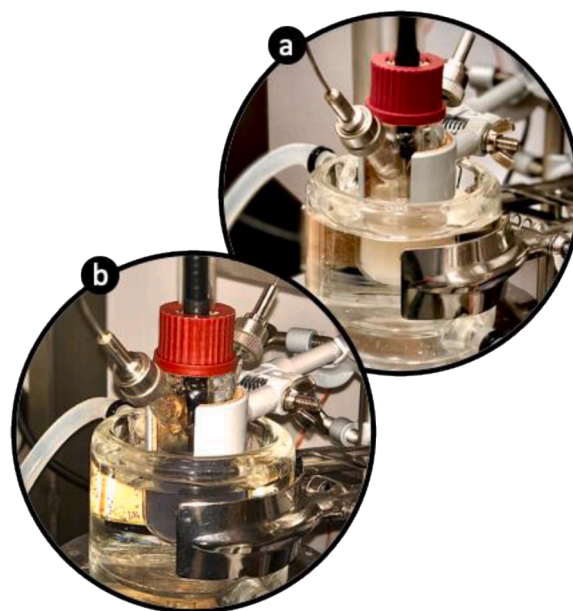


Fig. 8. The color of the P25-CuOx suspension prior and after 1 h of UV (365 nm) light irradiation.

in open air and the color changed gradually back to a white shaded one. The presence of the copper on the surface in different valences give rise to the generation of charge carriers upon the absorption of light, a phenomenon known as Localized Surface Plasmon Resonance (LSPR), which can be the reason behind the color changes during the experiments [37].

3.3. Photocatalytic selective biomass valorization

Titanium dioxide, and especially the commercially available P25, as well as functionalized materials based on TiO₂ are known for possessing an elevated photocatalytic decomposition efficiency against a wide range of organics. However, most of these processes are linked to the unselective transformation/mineralization of the reactant, most of the times organic pollutant. Going a step further, recent research efforts aim to utilize TiO₂ based materials for synthetic processes, such as the selective partial photo-oxidation of biomass derived compounds. In order to enhance the sustainability of the process, the addition of hazardous reagents/oxidants has been avoided in the present study. Furthermore, the two model compounds used for studying their selective partial photo-oxidative efficiency, are amongst the most valuable platform chemicals – intermediates derived from lignocellulosic biomass, i.e. 5-hydroxymethylfurfural (HMF) produced by cellulose derived glucose and the lignin derived benzyl alcohol (BnOH).

3.3.1. Photocatalytic selective partial oxidation of HMF to DFF

As it can be seen in Fig. 9, P25 achieved 100% HMF conversion after 3 h of UV light exposure, exhibiting however low DFF selectivity and yield. The highest values of DFF selectivity (21%) and yield (13%) were observed after 1 h of irradiation. The reactivity of the calcined P25 in converting HMF was similar to that of the parent P25. However, P25-400 showed higher selectivity (and yield) to DFF by about 5–10% compared to P25. These results reveal that the selective partial oxidation of HMF to DFF is not affected by the presence of surface water moieties. On the contrary, the transformation of the formed DFF moieties is affected, since DFF decomposes unselectively, with the latter not to be a desired effect. It should be pointed out that DFF does not get further oxidized to for instance 2,5-furandicarboxylic acid (FDCA) or other detected non-cyclic organics.

On the other hand, the copper modified photocatalyst showed a

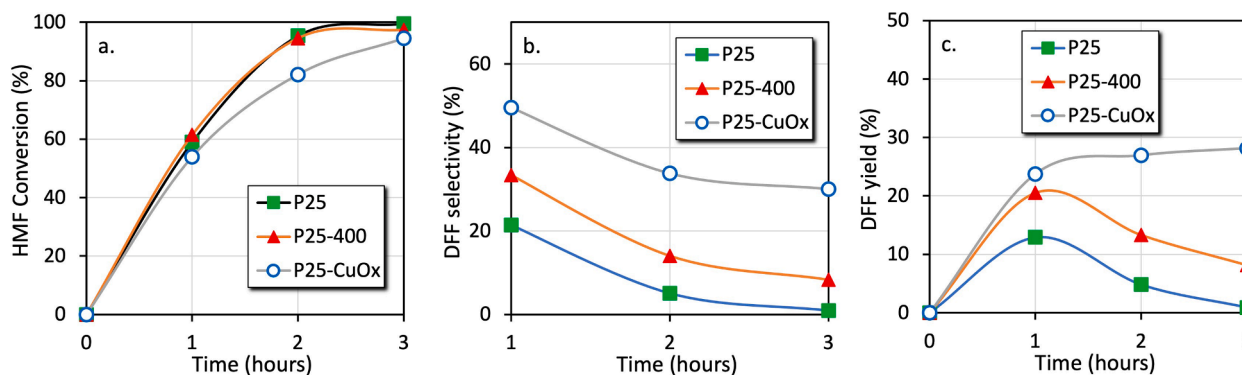


Fig. 9. HMF conversion (a), DFF selectivity (b), and DFF yield (c) for TiO₂-P25 (P25), TiO₂-P25 calcined in air at 400 °C (P25-400) and TiO₂-P25 decorated with ultra-nanoparticles of CuO_x (P25-CuOx) under ultraviolet irradiation at 30 °C (1 mM initial HMF in acetonitrile and 1 g/L loading of photocatalyst).

slightly lower HMF conversion at relatively longer reaction times (i.e. reaching 95% HMF conversion after 3 h), but the DFF selectivity was significantly higher in comparison to P25 and P25-400, i.e. 50 and 30% after 1 and 3 h of UV irradiation respectively. As a result, P25-CuOx presented the highest DFF yield of 30% after 3 h. It has to be pointed out that no other oxidation products like FDCA were detected, suggesting that the DFF was unselectively decomposed to low molecular weight organic compounds not detectable by LC-MS (like levulinic acid) or/and it was mineralized.

3.4. Photocatalytic selective partial oxidation of BnOH to PhCHO

Regarding the lignin derived model compound benzyl alcohol (BnOH), P25 showed a high conversion efficiency under UV light irradiation, reaching 97% of BnOH conversion within 3 h and >99% after 6 h (Fig. 10). The PhCHO selectivity and yield were moderate, being about 65–70% for the first 2 h of reaction and decreasing to about 32% after 6 h. The maximum PhCHO yield of 60% was observed at 2 h of reaction. P25-400 exhibited 95, 56, and 53% BnOH conversion, PhCHO selectivity and yield, respectively after 6 h. These results reveal that the removal of the strongly adsorbed surface water moieties led to faster reactivity since more catalytic sites are available. Moreover, the smaller amount of water favors the selectivity by lessening the further decomposition of the formed aldehyde to undesirable compounds. It is worth to mention that no other aromatic compounds like for instance benzoic acid were detected. Although, the decoration of the P25 nanoparticles with the ultra-nano CuO_x species had a negative impact on the BnOH conversion extend (81% after 6 h) and rate, the final PhCHO yield was 80%, a value more than two times higher than that of P25 and 51% higher comparing to P25-400. This high yield was attributed to the 100% PhCHO selectivity observed during the entire (6 h) photocatalytic experiment. This type of performance, i.e. stable 100% selectivity to the

targeted product at conversion $\geq 80\%$, is capable to support upscaled production processes by utilizing alternative approaches like microflow photoreactors decorated with P25-CuOx which can further boost the BnOH conversion.

3.5. The role of the CuO_x nanoclusters

The surface incorporated CuO_x nanoclusters have a bimodal role, since they can act either as active adsorption centers or/and as catalytic reduction sites. In general, it is well discussed that the photoexcited electron upon light irradiation are transferred from the conduction band (CB) of the TiO₂ phase to the Cu-clusters (delocalization) [18,36,67]. By this, the predominant drawback of fast charge recombination in the case of pure TiO₂ diminishes, while the Cu-clusters can act more reactively as redox catalytic sites. In the case of H₂ production, the holes are responsible for the formation of hydrogen ions (H⁺) from the oxidation of methanol [9,39,67]. The delocalized photoexcited e⁻ on the CuO_x phase are responsible for the reduction of H⁺ to molecular hydrogen [9].

Considering that the incorporation of the CuOx cluster led to a significant lower BnOH conversion rate, while in the case of HMF on the contrary the effect on the conversion was almost negligible, it can be assumed that the adsorption/interaction of the formed benzaldehyde on the CuO_x is not favorable. This can be a reason behind the fact that no further oxidation/decomposition of the formed benzaldehyde by the delocalized electrons on Cu clusters occurred, suggesting that the interaction of the aromatic benzyl alcohol is not thermodynamically favorable. In previous studies, it was presented that the organic moieties can either “strongly adsorbed” or “weakly adsorbed” on the surface and hence different mechanism of reaction occur [37]. We have presented similar mechanistic aspects in our previous studies [47,52,68], while we are investigating actively the involved oxidation pathways with the results to be presented in a forthcoming study. Regeneration of

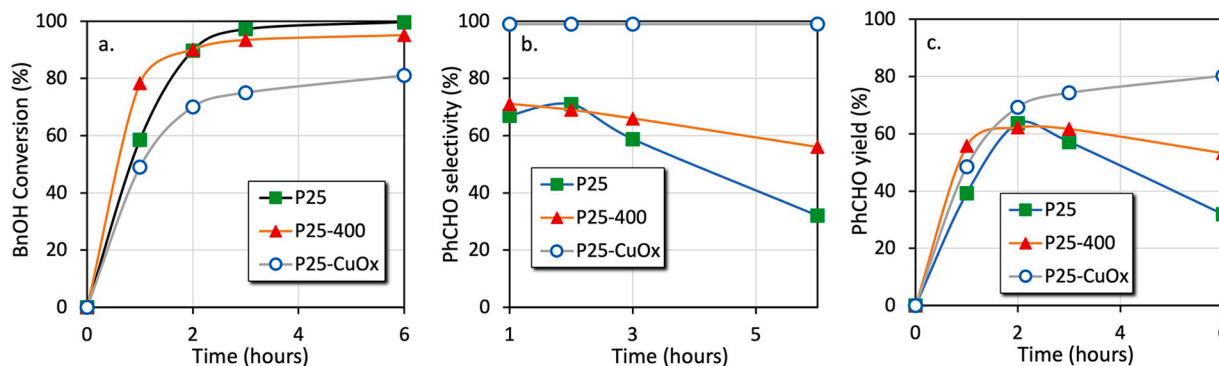


Fig. 10. BnOH conversion (a), PhCHO selectivity (b), and PhCHO yield (c) for TiO₂-P25 (P25), TiO₂-P25 calcined in air at 400 °C (P25-400) and TiO₂-P25 decorated with ultra-nanoparticles of CuO_x (P25-CuOx) under ultraviolet irradiation at 30 °C (1 mM initial BnOH in acetonitrile and 1 g/L loading of photocatalyst).

the P25-CuO_x nanocatalyst by washing the exhausted powder during filtration by water, methanol, and acetonitrile (100 mL of each sequentially) revealed that the photoreactivity was preserved, since the HMF and BnOH conversion after 3 h was less than 7% lower comparing to the initial experiments. Although, we would like to bring in attention that some defected sites of the materials surface is possible to be poisoned by the interactions of the organic compounds especially UV irradiation and we are actively researching towards this direction. Finally, a material that was synthesized following the same protocol but in silence conditions (no ultrasonication) showed lower HMF and BnOH conversion by ~10 and ~15%, respectively, and more importantly, the conversion deviation between different series of the same experiments ranged at around 15%, suggesting a lower extend of surface homogeneity/nanoclusters dispersion comparing to the ultrasound assisted synthesis.

4. Conclusions

The deposition of copper (~2.0% atomic content) on TiO₂ P25 by the use of an ultrasound-assisted ultra-wet (US-UWet) impregnation method resulted in the formation of homogeneously dispersed Cu nanoclusters of less than 4 nm, with the average diameter being 1.6 nm. These ultrananosized particles exhibit predominately as Cu₂O crystalline nanostructures, with minor contribution of CuO. The nanoengineered composite photocatalyst was efficient in H₂ production by water splitting using methanol as sacrificial agent under ultraviolet irradiation (365 nm) of a very low intensity, while the benchmark TiO₂ P25 did not reveal any photoreactivity to produce H₂. With regard to the application of the nanoclusters-decorated nanocatalyst in biomass valorization, the additives free partial photo-oxidation of two biomass derived model compounds, 5-hydroxymethylfurfural (HMF) and benzyl alcohol (BnOH) to value-added compounds, showed to be more selective and of a higher yield towards 2,5-diformylfuran (DFF) and benzaldehyde (PhCHO), respectively, compared to P25 and its calcinated counterpart. The elevated photoreactivity can be linked to the synergistic effect originated from the composite formation, with the more crucial derived phenomenon to be the nanosized homogeneous decoration of the spherical nanoclusters. The herein US-UWet impregnation synthesis can be assumed as a prosperous approach for the nanoparticles' decoration with nanoclusters of different chemical heterogeneities. Additionally, the exploration of the ultrasound effects by studying different frequencies and power can lead to novel multifunctional nano-photocatalysts for green oriented applications.

CRedit authorship contribution statement

Dimitrios A. Giannakoudakis: Writing – original draft, Investigation, Conceptualization, Visualization. **Abdul Qayyum:** Investigation. **Vaishakh Nair:** Investigation, Writing – review & editing. **Ayesha Khan:** Investigation. **Swaraj R. Pradhan:** Investigation. **Jovana Prekodravac:** Investigation, Writing – review & editing. **Kyriazis Rekos:** Investigation. **Alec P. LaGrow:** Formal analysis. **Oleksandr Bondarchuk:** Formal analysis. **Dariusz Łomot:** Methodology. **Konstantinos S. Triantafyllidis:** Writing – review & editing. **Juan Carlos Colmenares:** Writing – review & editing, Resources, Conceptualization, Project administration.

Declaration of Competing Interest

The authors declare that they have no known competing financial interests or personal relationships that could have appeared to influence the work reported in this paper.

Acknowledgments

DAG (www.dagchem.com), AQ, DL, and JCC (<http://photo-catalysis.org>) would like to acknowledge the support from the National Science center in Poland within OPUS-13 project nr 2017/25/B/ST8/01592. SRP and JCC want to acknowledge the National Science center in Poland within Sonata Bis 5 Project No. 2015/18/E/ST5/00306 for the support. Moreover, this publication is part of a project that has received funding from the European Union's Horizon 2020 research and innovation programme under the Marie Skłodowska-Curie grant agreement No. 711859 and from the financial resources for science in the years 2017-2021 awarded for the implementation of an international co-financed project. The authors would like to thank Dr. Dmytro Lisovytskiy for the samples' analysis by XRD. TEM and XPS experiments were carried out through the use of the INL Advanced Electron Microscopy, Imaging and Spectroscopy Facility.

Supplementary material associated with this article can be found, in the online version, at [doi:10.1016/j.mcat.2021.111664](https://doi.org/10.1016/j.mcat.2021.111664).

Supplementary materials

Supplementary material associated with this article can be found, in the online version, at [doi:10.1016/j.mcat.2021.111664](https://doi.org/10.1016/j.mcat.2021.111664).

References

- [1] B. You, X. Liu, N. Jiang, Y. Sun, A general strategy for decoupled hydrogen production from water splitting by integrating oxidative biomass valorization, *J. Am. Chem. Soc.* 138 (2016) 13639–13646, <https://doi.org/10.1021/jacs.6b07127>.
- [2] B. You, N. Jiang, X. Liu, Y. Sun, Simultaneous H₂ generation and biomass upgrading in water by an efficient noble-metal-free bifunctional electrocatalyst, *Angew. Chemie Int. Ed.* 55 (2016) 9913–9917, <https://doi.org/10.1002/anie.201603798>.
- [3] S. Sharma, S.K. Ghoshal, Hydrogen the future transportation fuel: from production to applications, *Renew. Sustain. Energy Rev.* 43 (2015) 1151–1158, <https://doi.org/10.1016/j.rser.2014.11.093>.
- [4] I. Godwin, A. Rovetta, M. Lyons, J. Coleman, Electrochemical water oxidation: the next five years, *Curr. Opin. Electrochem.* 7 (2018) 31–35, <https://doi.org/10.1016/j.coelec.2017.09.025>.
- [5] K.S. Triantafyllidis, A.A. Lappas, M. Stöcker, The Role of Catalysis for the Sustainable Production of Bio-Fuels and Bio-chemicals, Elsevier, 2013, <https://doi.org/10.1016/C2011-0-04285-0>.
- [6] V. Nair, M.J. Muñoz-Batista, M. Fernández-García, R. Luque, J.C. Colmenares, Thermo-photocatalysis: environmental and energy applications, *ChemSusChem.* 12 (2019) 2098–2116, <https://doi.org/10.1002/cssc.201900175>.
- [7] Y. Tan, Z. Shu, J. Zhou, T. Li, W. Wang, Z. Zhao, One-step synthesis of nanostructured g-C₃N₄/TiO₂ composite for highly enhanced visible-light photocatalytic H₂ evolution, *Appl. Catal. B* 230 (2018) 260–268, <https://doi.org/10.1016/j.apcatb.2018.02.056>.
- [8] S. Kumar, S. Karthikeyan, A. Lee, g-C₃N₄-Based nanomaterials for visible light-driven photocatalysis, *Catalysts* 8 (2018) 74, <https://doi.org/10.3390/catal8020074>.
- [9] T. Miwa, S. Kaneko, H. Katsumata, T. Suzuki, K. Ohta, S. Chand Verma, K. Sugihara, Photocatalytic hydrogen production from aqueous methanol solution with CuO/Al₂O₃/TiO₂ nanocomposite, *Int. J. Hydrog. Energy.* 35 (2010) 6554–6560, <https://doi.org/10.1016/j.ijhydene.2010.03.128>.
- [10] A. Akhundi, A. Badiei, G.M. Ziarani, A. Habibi-Yangjeh, M.J. Muñoz-Batista, R. Luque, Graphitic carbon nitride-based photocatalysts: toward efficient organic transformation for value-added chemicals production, *Mol. Catal.* 488 (2020), 110902, <https://doi.org/10.1016/j.mcat.2020.110902>.
- [11] O. Fontelles-Carceller, M.J. Muñoz-Batista, J.C. Conesa, A. Kubacka, M. Fernández-García, H₂ photo-production from methanol, ethanol and 2-propanol: pt-(Nb)TiO₂ performance under UV and visible light, *Mol. Catal.* 446 (2018) 88–97, <https://doi.org/10.1016/j.mcat.2017.12.023>.
- [12] G. Jiang, X. Yang, Y. Wu, Z. Li, Y. Han, X. Shen, A study of spherical TiO₂/g-C₃N₄ photocatalyst: morphology, chemical composition and photocatalytic performance in visible light, *Mol. Catal.* 432 (2017) 232–241, <https://doi.org/10.1016/j.mcat.2016.12.026>.
- [13] T. Lv, H. Wang, W. Hong, P. Wang, L. Jia, In situ self-assembly synthesis of sandwich-like TiO₂/reduced graphene oxide/LaFeO₃ Z-scheme ternary heterostructure towards enhanced photocatalytic hydrogen production, *Mol. Catal.* 475 (2019), 110497, <https://doi.org/10.1016/j.mcat.2019.110497>.
- [14] J.Y. Li, Y.H. Li, M.Y. Qi, Q. Lin, Z.R. Tang, Y.J. Xu, Selective organic transformations over cadmium sulfide-based photocatalysts, *ACS Catal.* 10 (2020) 6262–6280, <https://doi.org/10.1021/acscatal.0c01567>.
- [15] D. Strmenik, P.P. Lopes, B. Genorio, V.R. Stamenkovic, N.M. Markovic, Design principles for hydrogen evolution reaction catalyst materials, *Nano Energy* 29 (2016) 29–36, <https://doi.org/10.1016/j.nanoen.2016.04.017>.
- [16] K. Vikrant, K.H. Kim, F. Dong, D.A. Giannakoudakis, Photocatalytic platforms for removal of ammonia from gaseous and aqueous matrixes: status and challenges, *ACS Catal.* 10 (2020) 8683–8716, <https://doi.org/10.1021/acscatal.0c02163>.
- [17] Y.H. Li, F. Zhang, Y. Chen, J.Y. Li, Y.J. Xu, Photoredox-catalyzed biomass intermediate conversion integrated with H₂ production over Ti₃C₂T: x/CdS

- composites, *Green Chem.* 22 (2020) 163–169, <https://doi.org/10.1039/c9gc03332g>.
- [18] C. Castañeda, F. Tzompantzi, A. Rodríguez-Rodríguez, M. Sánchez-Domínguez, R. Gómez, Improved photocatalytic hydrogen production from methanol/water solution using CuO supported on fluorinated TiO₂, *J. Chem. Technol. Biotechnol.* 93 (2018) 1113–1120, <https://doi.org/10.1002/jctb.5470>.
- [19] Q. Lin, Y.H. Li, M.Y. Qi, J.Y. Li, Z.R. Tang, M. Anpo, Y.M.A. Yamada, Y.J. Xu, Photoredox dual reaction for selective alcohol oxidation and hydrogen evolution over nickel surface-modified ZnIn₂S₄, *Appl. Catal. B* 271 (2020), 118946, <https://doi.org/10.1016/j.apcatb.2020.118946>.
- [20] T.P. Nguyen, D.M. Tuan Nguyen, D.L. Tran, H.K. Le, D.V.N. Vo, S.S. Lam, R. S. Varma, M. Shokouhimehr, C.C. Nguyen, Q. Van Le, MXenes: applications in electrocatalytic, photocatalytic hydrogen evolution reaction and CO₂ reduction, *Mol. Catal.* 486 (2020), 110850, <https://doi.org/10.1016/j.mcat.2020.110850>.
- [21] V. Kumaravel, S. Mathew, J. Bartlett, S.C. Pillai, Photocatalytic hydrogen production using metal doped TiO₂: a review of recent advances, *Appl. Catal. B* 244 (2019) 1021–1064, <https://doi.org/10.1016/j.apcatb.2018.11.080>.
- [22] M. Sakar, C.C. Nguyen, M.H. Vu, T.O. Do, Materials and mechanisms of photo-assisted chemical reactions under light and dark conditions: can day–night photocatalysis be achieved? *ChemSusChem* 11 (2018) 809–820, <https://doi.org/10.1002/cssc.201702238>.
- [23] D.A. Giannakoudakis, G. Chatel, J.C. Colmenares, Mechanochemical forces as a synthetic tool for zero- and one-dimensional titanium oxide-based nanophotocatalysts, *Top. Curr. Chem.* 378 (2020) 2, <https://doi.org/10.1007/s41061-019-0262-3>.
- [24] N. Liu, X. Zhou, N.T. Nguyen, K. Peters, F. Zoller, I. Hwang, C. Schneider, M. E. Miehlich, D. Freitag, K. Meyer, D. Fattakhova-Rohlfing, P. Schmuki, Black magic in gray titania: noble-metal-free photocatalytic H₂ evolution from hydrogenated anatase, *ChemSusChem* 10 (2017) 62–67, <https://doi.org/10.1002/cssc.201601264>.
- [25] E. Da Costa, P.P. Zamora, A.J.G. Zarbin, Novel TiO₂/C nanocomposites: synthesis, characterization, and application as a photocatalyst for the degradation of organic pollutants, *J. Colloid Interface Sci.* 368 (2012) 121–127, <https://doi.org/10.1016/j.jcis.2011.10.028>.
- [26] X. Lin, D. Fu, L. Hao, Z. Ding, Synthesis and enhanced visible-light responsive of C, N,S-tridoped TiO₂ hollow spheres, *J. Environ. Sci.* 25 (2013) 2150–2156, [https://doi.org/10.1016/S1001-0742\(13\)60414-3](https://doi.org/10.1016/S1001-0742(13)60414-3).
- [27] D.A. Giannakoudakis, N. Farahmand, D. Łomot, K. Sobczak, T.J. Bandoz, J. C. Colmenares, Ultrasound-activated TiO₂/GO-based bifunctional photoreactive adsorbents for detoxification of chemical warfare agent surrogate vapors, *Chem. Eng. J.* 395 (2020), 125099, <https://doi.org/10.1016/j.cej.2020.125099>.
- [28] J. Guo, S. Zhu, Z. Chen, Y. Li, Z. Yu, Q. Liu, J. Li, C. Feng, D. Zhang, Sonochemical synthesis of TiO₂ nanoparticles on graphene for use as photocatalyst, *Ultrason. Sonochem.* 18 (2011) 1082–1090, <https://doi.org/10.1016/j.ultsonch.2011.03.021>.
- [29] T.D. Nguyen-Phan, V.H. Pham, E.W. Shin, H.D. Pham, S. Kim, J.S. Chung, E.J. Kim, S.H. Hur, The role of graphene oxide content on the adsorption-enhanced photocatalysis of titanium dioxide/graphene oxide composites, *Chem. Eng. J.* 170 (2011) 226–232, <https://doi.org/10.1016/j.cej.2011.03.060>.
- [30] C. Berberidou, G.Z. Kyzas, I. Paspaltsis, T. Sklavidiadis, I. Poulidis, Photocatalytic disinfection and purification of water employing reduced graphene oxide/TiO₂ composites, *J. Chem. Technol. Biotechnol.* 94 (2019) 3905–3914, <https://doi.org/10.1002/jctb.6188>.
- [31] W.H.M. Abdelraheem, M.K. Patil, M.N. Nadagouda, D.D. Dionysiou, Hydrothermal synthesis of photoactive nitrogen- and boron- codoped TiO₂ nanoparticles for the treatment of bisphenol A in wastewater: synthesis, photocatalytic activity, degradation byproducts and reaction pathways, *Appl. Catal. B* 241 (2019) 598–611, <https://doi.org/10.1016/j.apcatb.2018.09.039>.
- [32] D.A. Giannakoudakis, F. Pearsall, M. Florent, J. Lombardi, S. O'Brien, T.J. Bandoz, Barium titanate perovskite nanoparticles as a photoreactive medium for chemical warfare agent detoxification, *J. Colloid Interface Sci.* 531 (2018) 233–244, <https://doi.org/10.1016/j.jcis.2018.07.053>.
- [33] W.-C. Lin, W.-D. Yang, L.-L. Huang, T.-S. Wu, Z.-J. Chung, Hydrogen production from methanol/water photocatalytic decomposition using Pt/TiO₂-xNx catalyst, *Energy Fuels* 23 (2009) 2192–2196, <https://doi.org/10.1021/ef801091p>.
- [34] S. Oros-Ruiz, R. Zanella, R. López, A. Hernández-Gordillo, R. Gómez, Photocatalytic hydrogen production by water/methanol decomposition using Au/TiO₂ prepared by deposition-precipitation with urea, *J. Hazard. Mater.* 263 (2013) 2–10, <https://doi.org/10.1016/j.jhazmat.2013.03.057>.
- [35] N.L. De Silva, A.C.A. Jayasundera, A. Folger, O. Kasian, S. Zhang, C.-F. Yan, C. Scheu, J. Bandara, Superior solar-to-hydrogen energy conversion efficiency by visible light-driven hydrogen production via highly reduced Ti₂⁺/Ti₃⁺ states in blue titanium dioxide photocatalyst, *Catal. Sci. Technol.* 8 (2018) 4657–4664, <https://doi.org/10.1039/C8CY01212A>.
- [36] A.T. Montoya, E.G. Gillan, Enhanced photocatalytic hydrogen evolution from transition-metal surface-modified TiO₂, *ACS Omega* 3 (2018) 2947–2955, <https://doi.org/10.1021/acsomega.7b02021>.
- [37] L. Clarizia, G. Vitiello, G. Luciani, I. Di Somma, R. Andreozzi, R. Marotta, situ photodeposited nanoCu on TiO₂ as a catalyst for hydrogen production under UV/visible radiation, *Appl. Catal. A* 518 (2016) 142–149, <https://doi.org/10.1016/j.apcata.2015.07.044>.
- [38] J. Yu, J. Ran, Facile preparation and enhanced photocatalytic H₂-production activity of Cu(OH)₂ cluster modified TiO₂, *Energy Environ. Sci.* 4 (2011) 1364–1371, <https://doi.org/10.1039/c0ee00729c>.
- [39] H. Tian, X.L. Zhang, J. Scott, C. Ng, R. Amal, TiO₂-supported copper nanoparticles prepared via ion exchange for photocatalytic hydrogen production, *J. Mater. Chem. A* 2 (2014) 6432–6438, <https://doi.org/10.1039/C3TA15254E>.
- [40] J.C. Colmenares, R.S. Varma, V. Nair, Selective photocatalysis of lignin-inspired chemicals by integrating hybrid nanocatalysis in microfluidic reactors, *Chem. Soc. Rev.* 46 (2017) 6675–6686, <https://doi.org/10.1039/C7CS00257B>.
- [41] R. Rinaldi, R. Jastrzebski, M.T. Clough, J. Ralph, M. Kennema, P.C.A. Bruijninx, B. M. Weckhuysen, Paving the way for lignin valorisation: recent advances in bioengineering, *Bioresour. Catal.* 55 (2016) 8164–8215, <https://doi.org/10.1002/anie.201510351>.
- [42] L. Hu, L. Lin, Z. Wu, S. Zhou, S. Liu, Recent advances in catalytic transformation of biomass-derived 5-hydroxymethylfurfural into the innovative fuels and chemicals, *Renew. Sustain. Energy Rev.* 74 (2017) 230–257, <https://doi.org/10.1016/j.rser.2017.02.042>.
- [43] M.A. Kougiumtzis, A. Marianou, K. Atsonios, C. Michailof, N. Nikolopoulos, N. Koukouzas, K. Triantafyllidis, A. Lappas, E. Kakaras, Production of 5-HMF from cellulosic biomass: experimental results and integrated process simulation, *Waste Biomass Valor.* 9 (2018) 2433–2445, <https://doi.org/10.1007/s12649-018-0267-0>.
- [44] P. Lisowski, J.C. Colmenares, O. Mašek, W. Lisowski, D. Lisovyt'skiy, A. Kamińska, D. Łomot, Dual functionality of TiO₂/biochar hybrid materials: photocatalytic phenol degradation in the liquid phase and selective oxidation of methanol in the gas phase, *ACS Sustain. Chem. Eng.* 5 (2017) 6274–6287, <https://doi.org/10.1021/acssuschemeng.7b01251>.
- [45] J.C. Colmenares, P. Lisowski, D. Łomot, O. Chernyayeva, D. Lisovyt'skiy, Sonophotodeposition of bimetallic photocatalysts Pd-Au/TiO₂: application to selective oxidation of methanol to methyl formate, *ChemSusChem* 8 (2015) 1676–1685, <https://doi.org/10.1002/cssc.201403125>.
- [46] W. Ouyang, E. Kuna, A. Yezep, A. Balu, A. Romero, J. Colmenares, R. Luque, Mechanochemical synthesis of TiO₂ nanocomposites as photocatalysts for benzyl alcohol photo-oxidation, *Nanomaterials* 6 (2016) 93, <https://doi.org/10.3390/nano6050093>.
- [47] D.A. Giannakoudakis, D. Łomot, J.C. Colmenares, When sonochemistry meets heterogeneous photocatalysis: designing a sonophotoreactor towards sustainable selective oxidation, *Green Chem.* 22 (2020) 4896–4905, <https://doi.org/10.1039/D0GC00329H>.
- [48] U. Diebold, The surface science of titanium dioxide, *Surf. Sci. Rep.* 48 (2003) 53–229, [https://doi.org/10.1016/S0167-5729\(02\)00100-0](https://doi.org/10.1016/S0167-5729(02)00100-0).
- [49] H. Hamad, E. Bailón-García, F.F. Maldonado-Hódar, A.F. Pérez-Cadenas, F. Carrasco-Marín, S. Morales-Torres, Synthesis of TiO₂nanocrystals in mild synthesis conditions for the degradation of pollutants under solar light, *Appl. Catal. B Environ.* 241 (2019) 385–392, <https://doi.org/10.1016/j.apcatb.2018.09.016>.
- [50] S. Rajoriya, S. Bargole, S. George, V.K. Saharan, P.R. Gogate, A.B. Pandit, Synthesis and characterization of samarium and nitrogen doped TiO₂ photocatalysts for photo-degradation of 4-acetamidophenol in combination with hydrodynamic and acoustic cavitation, *Sep. Purif. Technol.* 209 (2019) 254–269, <https://doi.org/10.1016/j.seppur.2018.07.036>.
- [51] W. Li, M. Liu, S. Feng, X. Li, J. Wang, D. Shen, Y. Li, Z. Sun, A.A. Elzatahy, H. Lu, D. Zhao, Template-free synthesis of uniform magnetic mesoporous TiO₂ nanospindles for highly selective enrichment of phosphopeptides, *Mater. Horizons.* 1 (2014) 439–445, <https://doi.org/10.1039/c4mh00030g>.
- [52] D.A. Giannakoudakis, A. Qayyum, D. Łomot, M.O. Besenhard, D. Lisovyt'skiy, T. J. Bandoz, J.C. Colmenares, Boosting the photoactivity of grafted titania: ultrasound-driven synthesis of a multi-phase heterogeneous nano-architected photocatalyst, *Adv. Funct. Mater.* 31 (2021), 2007115, <https://doi.org/10.1002/adfm.202007115>.
- [53] J. Guo, X. Cai, Y. Li, R. Zhai, S. Zhou, P. Na, The preparation and characterization of a three-dimensional titanium dioxide nanostructure with high surface hydroxyl group density and high performance in water treatment, *Chem. Eng. J.* 221 (2013) 342–352, <https://doi.org/10.1016/j.cej.2013.02.005>.
- [54] C.-Y. Wu, K.-J. Tu, J.-P. Deng, Y.-S. Lo, C.-H. Wu, Markedly enhanced surface hydroxyl groups of TiO₂ nanoparticles with superior water-dispersibility for photocatalysis, *Materials* 10 (2017) 566, <https://doi.org/10.3390/ma10050566>.
- [55] J. Chen, Z. Ding, C. Wang, H. Hou, Y. Zhang, C. Wang, G. Zou, X. Ji, Black anatase titania with ultrafast sodium-storage performances stimulated by oxygen vacancies, *ACS Appl. Mater. Interfaces.* 8 (2016) 9142–9151, <https://doi.org/10.1021/acsami.6b01183>.
- [56] T.J. Bandoz, A. Policicchio, M. Florent, P.S. Poon, J. Matos, TiO₂/S-doped carbons hybrids: analysis of their interfacial and surface features, *Molecules* 24 (2019) 3585, <https://doi.org/10.3390/molecules24193585>.
- [57] D.A. Giannakoudakis, M. Barczak, M. Florent, T.J. Bandoz, Analysis of interactions of mustard gas surrogate vapors with porous carbon textiles, *Chem. Eng. J.* 362 (2019) 758–766, <https://doi.org/10.1016/j.cej.2019.01.064>.
- [58] Z. Ai, N. Wu, L. Zhang, A nonaqueous sol-gel route to highly water dispersible TiO₂ nanocrystals with superior photocatalytic performance, *Catal. Today.* 224 (2014) 180–187, <https://doi.org/10.1016/j.cattod.2013.10.030>.
- [59] C. Yang, J. Qin, Z. Xue, M. Ma, X. Zhang, R. Liu, Rational design of carbon-doped TiO₂ modified g-C₃N₄ via in-situ heat treatment for drastically improved photocatalytic hydrogen with excellent photostability, *Nano Energy* 41 (2017) 1–9, <https://doi.org/10.1016/j.nanoen.2017.09.012>.
- [60] M. Salavati-Niasari, F. Davar, Synthesis of copper and copper(I) oxide nanoparticles by thermal decomposition of a new precursor, *Mater. Lett.* 63 (2009) 441–443, <https://doi.org/10.1016/j.matlet.2008.11.023>.
- [61] H.-L. Chen, T.-H. Chiang, M.-C. Wu, Evolution of morphology of nano-scale CuO grown on copper metal sheets in 5 wt% NaCl solution of spray fog environment,

- J. Surf. Eng. Mater. Adv. Technol. 02 (2012) 278–283, <https://doi.org/10.4236/jsemat.2012.24042>.
- [62] M. Verma, V.K. Gupta, V. Dave, R. Chandra, G.K. Prasad, Synthesis of sputter deposited CuO nanoparticles and their use for decontamination of 2-chloroethyl ethyl sulfide (CEES), *J. Colloid Interface Sci.* 438 (2015) 102–109, <https://doi.org/10.1016/j.jcis.2014.09.060>.
- [63] M. Verma, V.K. Gupta, V. Dave, R. Chandra, G.K. Prasad, Synthesis of sputter deposited CuO nanoparticles and their use for decontamination of 2-chloroethyl ethyl sulfide (CEES), *J. Colloid Interface Sci.* 438 (2015) 102–109, <https://doi.org/10.1016/j.jcis.2014.09.060>.
- [64] J.F. Guayaquil-Sosa, B. Serrano-Rosales, P.J. Valadés-Pelayo, H. de Lasa, Photocatalytic hydrogen production using mesoporous TiO₂ doped with Pt, *Appl. Catal. B* 211 (2017) 337–348, <https://doi.org/10.1016/j.apcatb.2017.04.029>.
- [65] P. Kubelka, F. Munk, Reflection characteristics of paints, *Z. Tech. Phys.* 12 (1931) 593–601.
- [66] S.M. Gupta, M. Tripathi, A review of TiO₂ nanoparticles, *Chinese Sci. Bull.* 56 (2011) 1639–1657, <https://doi.org/10.1007/s11434-011-4476-1>.
- [67] P. Gomathisankar, T. Noda, H. Katsumata, T. Suzuki, S. Kaneco, Enhanced hydrogen production from aqueous methanol solution using TiO₂/Cu as photocatalysts, *Front. Chem. Sci. Eng.* 8 (2014) 197–202, <https://doi.org/10.1007/s11705-014-1417-y>.
- [68] S.R. Pradhan, V. Nair, D.A. Giannakoudakis, D. Lisovvtskiy, J.C. Colmenares, Design and development of TiO₂ coated microflow reactor for photocatalytic partial oxidation of benzyl alcohol, *Mol. Catal.* 486 (2020), 110884, <https://doi.org/10.1016/j.mcat.2020.110884>.